Biointerface Research in Applied Chemistry
Open-Access Journal (ISSN: 2069-5837)

Article
Volume 16, Issue 3, 2026, 80
https://doi.org/10.33263/BRIAC163.080

Multi-level Computational Screening of Withanolides from *Physalis philadelphica* for Renal Adenocarcinoma Therapeutics

Hung Duc Nguyen [1,*]

[1] Faculty of Biology, Thai Nguyen University of Education, Thai Nguyen, 24124, Viet Nam
* Correspondence: hungnd@tnue.edu.vn;

Received: 24.02.2026; Accepted: 20.05.2026; Published: 15.06.2026

Abstract: Renal cell carcinoma, particularly advanced clear-cell disease, continues to require new mechanism-guided therapeutic options. Withanolides from Physalis philadelphica represent a structurally diverse natural-product class with reported cytotoxicity, but target-level mechanisms remain insufficiently defined. The present study performed a multi-level in silico evaluation of selected withanolides from *Physalis philadelphica* against the anti-apoptotic protein Mcl-1 (PDB: 6QFQ), using Belzutifan as a comparative reference. Docking analysis identified withaphysacarpin (CPD2) as the top-ranked candidate, with a predicted affinity more favorable than that of Belzutifan and a BH3-groove contact pattern dominated by hydrophobic and van der Waals interactions. Subsequent 100 ns molecular dynamics simulations supported the dynamic stability of the CPD2-6QFQ and Belzutifan-6QFQ complexes, with preserved backbone stability, compactness, and limited local fluctuations. MMGBSA analysis further favored CPD2 over Belzutifan, with a more favorable predicted binding profile driven mainly by nonpolar packing and a lower solvation penalty. ADMET prediction suggested a mixed developability profile for CPD2, including a comparatively favorable CYP inhibition pattern alongside an AMES mutagenicity alert. Current findings support CPD2 as a computationally prioritized candidate scaffold for Mcl-1-directed RCC research, while emphasizing the need for biochemical target validation, cellular apoptosis assays, selectivity profiling, and confirmatory safety testing.

Keywords: anti-apoptosis; DFT; Mcl-1; molecular modeling; renal adenocarcinoma; withanolide.

© 2026 by the authors. This article is an open-access article distributed under the terms and conditions of the Creative Commons Attribution (CC BY) license (https://creativecommons.org/licenses/by/4.0/), which permits unrestricted use, distribution, and reproduction in any medium, provided the original work is properly cited. The authors retain copyright of their work, and no permission is required from the authors or the publisher to reuse or distribute this article, as long as proper attribution is given to the original source.

1. Introduction

Renal cell carcinoma (RCC) remains a major oncologic challenge due to its high mortality rate and continues to require improved therapeutic strategies, particularly for advanced disease [1]. Recent clinical reviews describe RCC as a common malignancy with substantial global incidence, with clear-cell RCC representing the predominant histologic subtype and the major focus of systemic targeted therapy development [2]. Contemporary management has expanded with immune checkpoint inhibitor combinations and targeted agents, while unmet needs persist in treatment sequencing, resistance control, and durable disease suppression in advanced settings [3]. Belzutifan, an FDA-approved small-molecule inhibitor, has significantly changed the therapeutic landscape for advanced RCC, further underscoring the clinical relevance of mechanism-guided small-molecule discovery in renal cancer research [4].

Apoptosis dysregulation contributes to tumor persistence and therapeutic resistance in RCC, and anti-apoptotic Bcl-2 family members remain attractive targets for intervention [5]. Mcl-1 has received sustained attention because of its anti-apoptotic function, resistance-associated signaling roles, and structural features centered on the BH3-binding groove that support structure-based inhibitor design while still presenting medicinal-chemistry challenges. Recent cancer-focused and RCC-relevant literature further supports continued evaluation of Mcl-1-directed strategies, including biomarker-linked susceptibility contexts in clear-cell renal cancer [6,7].

Natural products remain a productive source of anticancer lead scaffolds, and withanolides constitute a chemically rich class with broad cytotoxic and mechanistically diverse antitumor activities reported across multiple cancer models. Contemporary reviews also describe withanolides as promising anticancer candidates while emphasizing the need for target-focused mechanistic validation and pharmacokinetic risk assessment [8,9]. The genus *Physalis* represents an established reservoir of withanolide metabolites, and recent phytochemical studies on *Physalis philadelphica* reported numerous withanolides possessing cytotoxic activity against renal adenocarcinoma (ACHN cell line) [10]. However, the mechanisms of action of these compounds have not been fully elucidated, creating an important knowledge gap and motivating target-oriented computational screening to prioritize withanolide candidates for further mechanistic and experimental validation in RCC.

In this study, a multi-level computational approach was applied to prioritize selected withanolides from *P. philadelphica* for their potential interaction with the anti-apoptotic target Mcl-1 in a renal adenocarcinoma-relevant context. The workflow integrated molecular docking for pose generation and preliminary affinity ranking, molecular dynamics simulations for time-resolved stability assessment of docked complexes, MMGBSA-based end-state free-energy estimation for comparative energetic refinement, and ADMET prediction for early pharmacokinetic and toxicity risk assessment. Together, this strategy provides a hypothesis-driven framework for withanolides as candidate Mcl-1 modulators for subsequent mechanistic and experimental validations in RCC models.

2. Materials and Methods

2.1. Structural preparation of selected ligands.

The selected withanolides possessing significant cytotoxic activity against renal adenocarcinoma (ACHN cell line) [10], including 17-*epi*-philadelphicalactone (CPD1), withaphysacarpin (CPD2), philadelphicalactone C (CPD3), ixocarpalactone A (CPD4), and withanolide E (CPD5), have molecular formulas of $C_{40}H_{40}O_8$ and $C_{40}H_{38}O_9$, respectively, with molecular weights of 488.2774, 488.2774, 488.2774, 504.2723, and 486.2618 Da. The Belzutifan, possessing a molecular formula of $C_{17}H_{12}F_3NO_4S$ and a molecular weight of 383.0439 Da, was chosen as the comparative reference (Figure 1).

(a) **(b)** **(c)**

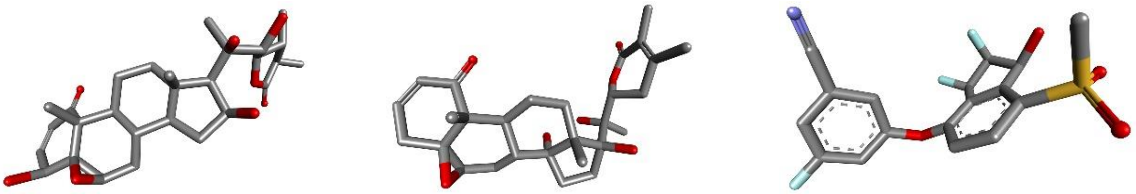

(d) **(e)** **(f)**

Figure 1. 3D Structures of selected ligands. **(a)** CPD1; **(b)** CPD2; **(c)** CPD3; **(d)** CPD4; **(e)** CPD5; **(f)** Belzutifan.

2.2. Molecular docking.

Three-dimensional geometries of the selected ligands were prepared in PDB format using BIOVIA Discovery Studio Visualizer. The preparation workflow included adding polar hydrogens, assigning Gasteiger partial charges, and defining rotatable torsional bonds to permit conformational flexibility. The Mcl-1 protein structure (PDB ID: 6QFQ) was retrieved in PDB format from the RCSB Protein Data Bank [11]. Molecular docking between ligands and the target protein was conducted with AutoDock Tools. A grid box comprising 60 points along each of the x, y, and z axes with a spacing of 0.375 Å was applied, centered at x = 3.934 Å, y = -18.337 Å, and z = 18.685 Å on the 6QFQ structure. The grid configuration was designed to fully cover the binding region of interest, including residues capable of accommodating diverse ligand chemotypes, while providing adequate volume for ligand translation and rotation at a feasible computational cost. In AutoDock Tools, the scoring strategy relies on a semi-empirical free-energy-based function coupled with partial-charge assignment to estimate binding free energies and rank docking poses. Conformational searching was performed using the Lamarckian genetic algorithm to identify low-energy binding modes with improved interaction stability. After docking, the pose with the most favorable predicted affinity was examined in Discovery Studio Client 2024 and benchmarked against docking results for Belzutifan on the same protein, enabling a relative assessment of binding tendencies.

2.3. Molecular dynamics simulations.

Molecular dynamics simulations were conducted for the selected docked complexes of the 6QFQ protein over 100 ns using GROMACS 2024.4 [12]. The protein structure was curated to resolve missing atoms and residues with Swiss-PdbViewer [13], while ligand topology and parameters were generated via SwissParam [14]. The protein-ligand complex was placed in a periodic simulation box and solvated with TIP3P water containing 0.15 M NaCl. System neutralization and relaxation were performed by energy minimization for 50,000 steps. Equilibration was carried out in two stages: 100 ps under the NVT ensemble, followed by 100 ps under the NPT ensemble at 300 K and 1.0 bar. Temperature was regulated using the V-rescale thermostat, whereas pressure coupling was applied using the Berendsen barostat during equilibration and the Parrinello-Rahman barostat during the production phase. A single 100 ns production simulation was then performed with a 2 fs integration time step. Long-range electrostatics were treated using the particle-mesh Ewald method, and a 1.2 nm cutoff was applied to both Coulombic and van der Waals interactions in real space. All bonds involving hydrogen atoms were constrained using the LINCS algorithm. Trajectory frames were saved at 10 ps intervals for subsequent analysis. Post-simulation analyses were processed with Grace software to obtain root mean square deviation (RMSD), residue-specific root mean square fluctuation (RMSF), radius of gyration (Rg), number of hydrogen bonds (Hbonds), and solvent-

accessible surface area (SASA). Conformational comparisons and structural alignments were further examined in UCSF Chimera 1.13.3 [15]. In addition, ligand poses at 0 ns and 100 ns were superimposed within the protein active site to assess the persistence of key contacts, including hydrogen bonds, van der Waals interactions, and hydrophobic interactions, throughout the simulation, thereby characterizing interaction stability and binding endurance over the 100 ns simulation.

2.4. Molecular mechanics generalized born surface area (MMGBSA) analysis.

MMGBSA binding free-energy estimation was performed with the gmx_MMPBSA tool using the CHARMM36 force field to evaluate the CPD2-6QFQ and Belzutifan-6QFQ complexes. Polar solvation contributions were evaluated using the Generalized Born model, whereas nonpolar solvation terms were estimated from solvent-accessible surface area (SASA). Energy analysis was performed on snapshots extracted from the 20-100 ns interval of the MD trajectory. In the present workflow, 125 frames were included in the final MMGBSA calculation using the gmx_MMPBSA input file together with em.tpr, index.ndx, topol.top, and md_0_10_center.xtc. The main calculation settings included startframe = 2000, endframe = 10000, interval = 80, verbose = 2, and igb = 5. The resulting energy components were averaged to compare the relative binding behavior of the analyzed complexes under the same computational protocol.

2.5. Assay protocol for ADMET prediction.

ADMET (Absorption, Distribution, Metabolism, Excretion, and Toxicity) assessment is a key filtering step in drug-discovery pipelines because it can flag unfavorable pharmacokinetic behavior and safety concerns before resource-intensive development, thereby reducing attrition in later phases and supporting rational compound prioritization. In this study, the pkCSM web server was employed to predict ADMET-related parameters for CPD2 and Belzutifan. pkCSM relies on graph-based molecular signatures to infer descriptors for absorption, distribution, metabolism, excretion, and toxicity, enabling an organized in silico comparison of developability-relevant features across the evaluated candidates [16].

3. Results and Discussion

3.1. Molecular docking analysis.

Molecular docking is an essential *in silico*, structure-based method that predicts the preferred orientation and binding affinity of a ligand within a macromolecular target's binding site. It enables virtual screening, hit identification, and lead optimization by simulating molecular recognition, allowing researchers to evaluate compound interactions at the atomic level [17]. Within apoptosis-focused anticancer research, pro-survival Bcl-2 family proteins, particularly Mcl-1, function as central regulators of mitochondrial cell-death control, and small-molecule disruption of the BH3-binding groove represents an established therapeutic concept supported by extensive structural and translational literature [18]. The docking setup for 6QFQ was validated by redocking the co-crystallized ligand. The resulting pose closely matched the crystallographic orientation of J3E, with an RMSD of 1.1256 Å (Figure 2). This result supports the reliability of the docking protocol, since RMSD values below 2 Å are commonly considered acceptable [19].

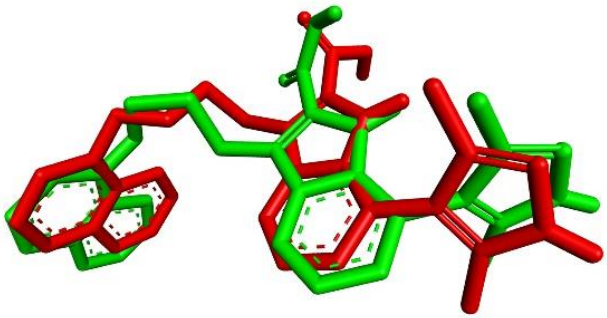

Figure 2. Superimposition of the docked and native ligands for validation of the molecular docking protocol (red = native, green = docked).

Predicted binding energies and principal non-covalent contacts for CPD1-CPD5 and the reference ligand Belzutifan against the 6QFQ target structure are summarized in Table 1.

Table 1. The interactions between the docked ligands and the protein 6QFQ.

Docked ligands	Binding energy (kcal/mol)	Hydrogen bond	Van der Waals interaction	Hydrophobic interaction
CPD1	-8.57	-	Ala227, Phe228, Ser247, Val249, Phe254, Thr266, Gly271	Met231, Leu235,Leu246, Met250, Val253, Leu267, Phe270, Val274, Leu290, Ile294
CPD2	-11.11	-	Phe228, Met231, Leu235, Leu246, Phe254, Arg263, Thr266, Gly271, Ser293	Val249, Met250, Val253, Leu267, Phe270, Val274, Leu290, Ile294
CPD3	-9.49	-	Phe228, Leu246, Phe254, Arg263, Thr266, Leu267, Gly271, Leu290, Ile294	Met231, Leu235, Val249, Met250, Val253, Phe270, Val274
CPD4	-8.86	Met250	His224, Ala227, Phe228, Leu235, Ile237, Leu246, Val249, Phe254, Thr266, Gly271, Leu290	Met231, Met250, Val253, Leu267, Phe270, Val274, Ile294
CPD5	-8.75	Leu267, Gly271	His224, Phe228, Met231, Ile237, Val249, Phe254, Thr266	Ala227, Leu235, Leu246, Met250, Val253, Leu267, Phe270, Val274, Leu290, Ile294
Belzutifan	-9.48	Met250, Arg263	Phe228, Leu235, Val253, Phe254, Gly271, Val274, Leu290, Ile294	Met231, Leu246, Val249, Met250, Thr266, Leu267, Phe270

The most favorable docking score was obtained for CPD2 (-11.11 kcal/mol), exceeding the reference Belzutifan (-9.48 kcal/mol) and the remaining candidates (CPD3: -9.49 kcal/mol; CPD4: -8.86 kcal/mol; CPD5: -8.75 kcal/mol; CPD1: -8.57 kcal/mol). Under a consistent scoring protocol, lower negative energies typically indicate a stronger predicted binding propensity, while absolute values are not transferable across distinct docking setups [20]. Residue-level inspection indicated that CPD2 occupied a canonical BH3-groove region on 6QFQ, engaging a recurrent cluster comprising Phe228, Met231, Val249, Met250, Val253, Arg263, Ile267, Phe270, and Gly271, residues frequently observed across crystallographic and medicinal-chemistry efforts directed toward Mcl-1 inhibition (Figure 3a) [21]. Despite absence of a hydrogen bond in the CPD2 pose, broad Van der Waals interactions were predicted (Phe228, Met231, Leu235, Leu246, Phe254, Arg263, Thr266, Gly271, Ser293), accompanied by an extensive hydrophobic interaction footprint (Val249, Met250, Val253, Leu267, Phe270, Val274, Leu290, Ile294). Such a pattern aligns with general interaction statistics from protein-ligand structural datasets, where hydrophobic packing and dispersion-driven complementarity frequently dominate stabilization within apolar grooves, with polar anchoring becoming optional rather than obligatory for high-scoring poses [22-24].

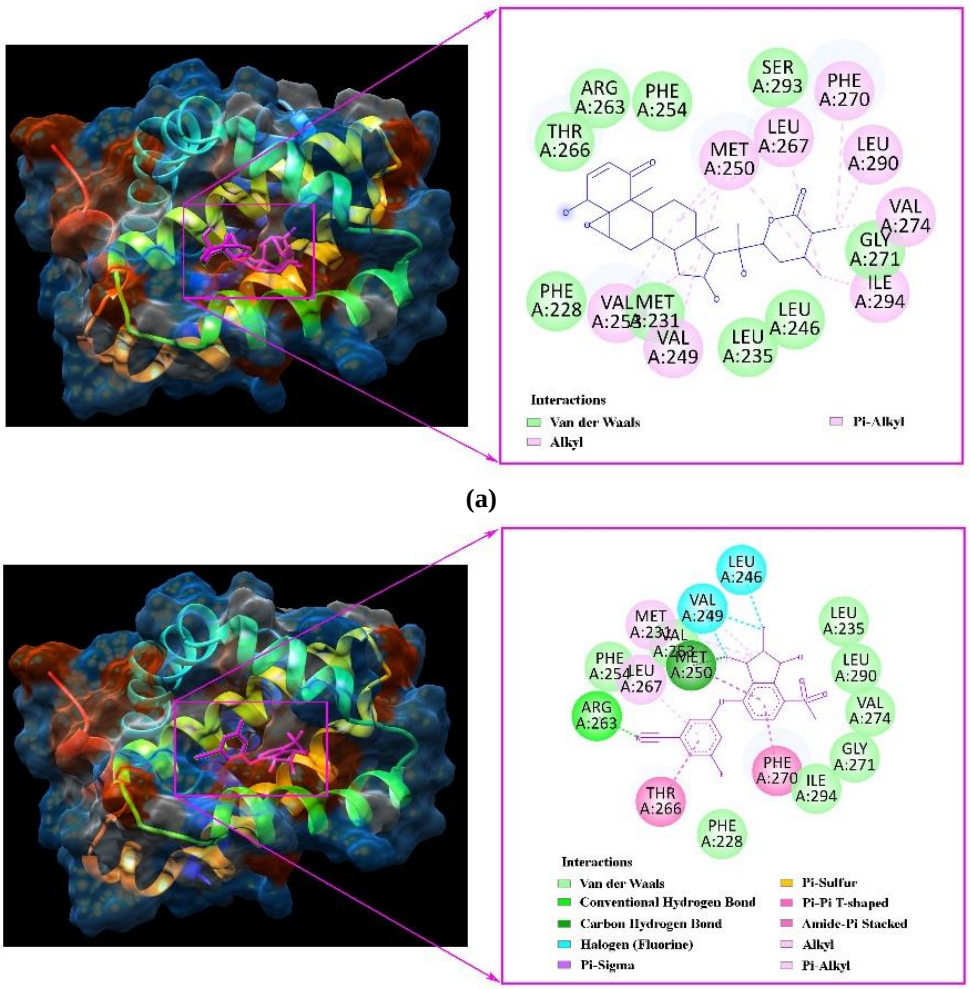

Figure 3. Molecular docking model and 2D interaction diagram of **(a)** CPD2; **(b)** Belzutifan with 6QFQ protein.

Belzutifan displayed a partially overlapping interaction map centered on Phe228, Met231, Val249, Met250, Val253, Arg263, Ile267, Phe270, and Gly271, including hydrogen bond formation with Met250 and Arg263, plus additional Van der Waals interaction and hydrophobic interaction contributions involving Leu235, Leu246, Thr266, Val274, Leu290, and Ile294 (Figure 3b). This overlap supports pocket-level comparability between CPD2 and Belzutifan within the same binding site [25,26]. For the remaining ligands, CPD3 showed a favorable score comparable to Belzutifan. It maintained BH3-groove engagement via Van der Waals interactions (Phe228, Leu246, Phe254, Arg263, Thr266, Leu267, Gly271, Leu290, Ile294) and hydrophobic interactions (Met231, Leu235, Val249, Met250, Val253, Phe270, Val274) without hydrogen-bond involvement, again suggesting the dominance of pocket-filling complementarity. CPD4 and CPD5 introduced polar anchoring while preserving extensive networks of Van der Waals and hydrophobic interactions across His224, Ala227, Phe228, Met231, Val249, Met250, Val253, Ile267, and Phe270. The presence of a Hydrogen bond in CPD4-CPD5, alongside weaker docking energies relative to CPD2, supports an interpretation in which hydrophobic burial and dispersion complementarity exert a greater influence than isolated polar contacts within this groove-like pocket, consistent with modern physical descriptions of binding in partially solvent-shielded hydrophobic clefts [27].

Overall, CPD2 emerged as the top-ranked candidate based on docking energy and a pocket-spanning contact pattern that substantially overlaps the Belzutifan interaction region,

supporting prioritizing CPD2 for molecular dynamics simulations and downstream endpoint free-energy validation. Such a progression follows prevailing guidance for Bcl-2 family targets, where conformational adaptation and interaction persistence across simulations can refine rankings derived from rigid or semi-flexible docking. Taken together, these docking results suggest that the predicted advantage of CPD2 may depend more on groove complementarity and nonpolar packing than on discrete hydrogen-bond anchoring. This interpretation is consistent with the hydrophobic character of the BH3-binding region. However, docking scores should still be regarded as protocol-dependent ranking outputs rather than direct measures of experimental binding affinity.

3.2. Molecular dynamics simulations.

Molecular dynamics simulations serve as a crucial post-docking validation tool in computational drug discovery by addressing the limitations of static molecular docking. While docking rapidly screens large libraries to identify potential binding poses, molecular dynamics provides an atomistic, time-resolved, and thermodynamically relevant assessment of those poses under physiological conditions, typically using explicit-solvent models [28]. Accordingly, trajectory-based descriptors and energy terms were extracted from the equilibrated simulations to quantify whether the docked binding modes remained conformationally stable and solvent-adapted over time. Therefore, the evaluation systematically investigated RMSD, RMSF, Rg, Hbonds, and SASA metrics to determine the stability, flexibility, and solvent exposure of the CPD2-6QFQ and Belzutifan-6QFQ complexes throughout the simulation timeframe. Consequently, the total energy and potential energy values for the CPD2-6QFQ complex were found to be -219,643 kJ/mol and -273,640 kJ/mol, respectively. For the Belzutifan-6QFQ complex, the total energy and potential energy values were measured to be -221,159 kJ/mol and -275,106 kJ/mol, respectively. The simulation system maintained equilibrium at 300 K.

Backbone RMSD traces for CPD2-6QFQ and Belzutifan-6QFQ remained within a narrow sub-nanometer envelope across 100 ns (approximately 0.08-0.16 nm), supporting preservation of the overall fold without sustained drift compatible with large-scale destabilization (Figure 4a). A rapid rise during the early portion of the trajectory was followed by fluctuations around a quasi-stationary band, consistent with relaxation from the initial docked geometry into a thermally adapted ensemble. The two profiles overlapped extensively; transient elevations occurred intermittently, yet neither complex displayed a monotonic increase at late times. Such RMSD behavior is commonly interpreted as the protein backbone's conformational stability during ligand-bound sampling, while acknowledging its sensitivity to alignment protocol and reference selection [29].

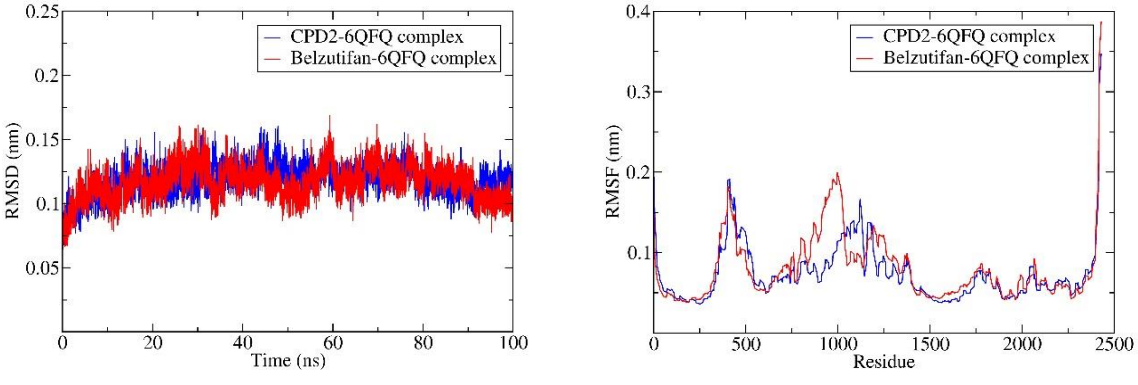

(a) **(b)**

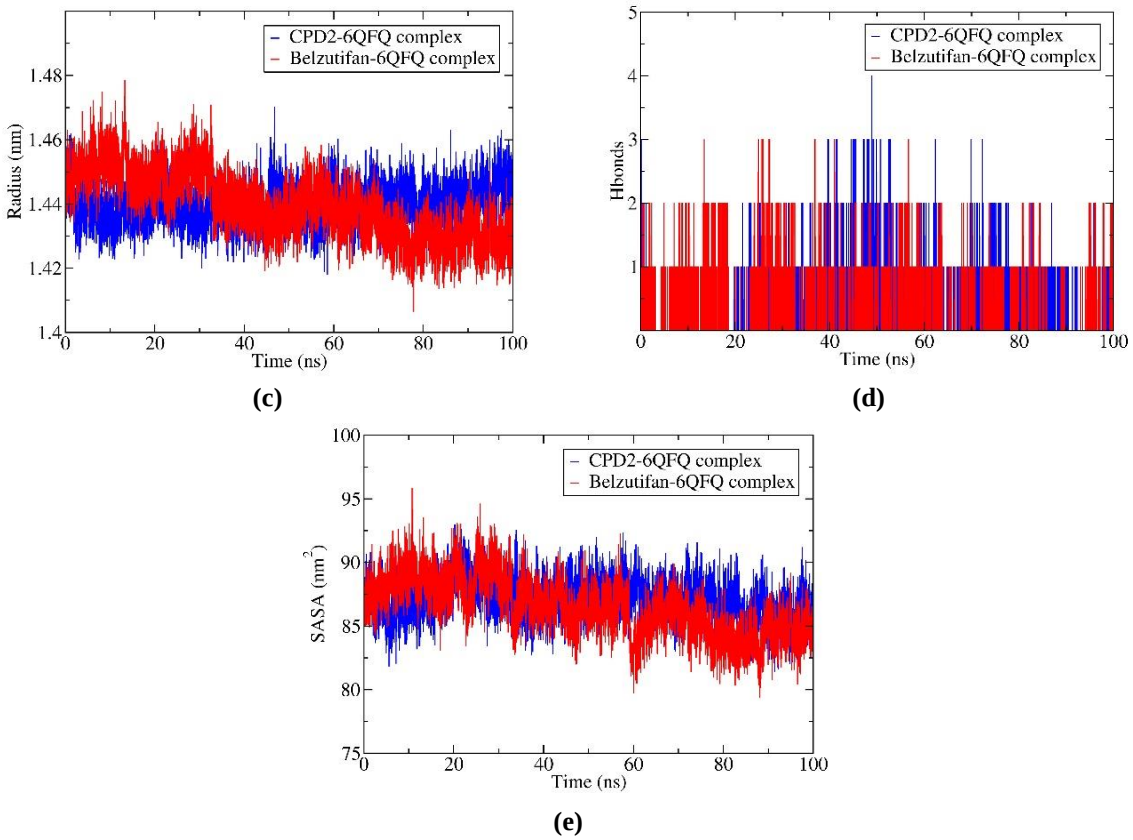

Figure 4. Results of MD simulation for the bindings of CPD2 (blue) and Belzutifan (red) with 6QFQ protein. **(a)** RMSD; **(b)** RMSF; **(c)** Rg; **(d)** Hbonds; **(e)** SASA.

Residue-level flexibility analysis focused on the Asp172-Val321 region indicated low-amplitude fluctuations overall, with RMSF values largely clustered near baseline (generally below 0.10 nm for most residues in this segment) (Figure 4b). Subtle trace separation appeared sporadically, with slightly elevated fluctuations in portions of the segment that include the binding-groove neighborhood (notably around His224-Val274). No sharp peak consistent with a localized unfolding-like event was observed within Asp172-Val321. This restrained mobility pattern supports a binding-site environment dominated by stable secondary-structure scaffolding and limited micro-rearrangements rather than pronounced local destabilization. RMSF-based interpretation of local flexibility in molecular dynamics trajectories is widely used to contextualize whether ligand accommodation coincides with stabilization or enhanced mobility of binding-proximal residues [30].

Radius of gyration (Rg) profiles for both complexes remained confined to a tight range (approximately 1.42-1.47 nm), indicating broadly stable global compactness throughout the simulation. Belzutifan-6QFQ sampled slightly higher Rg values during the earlier part of the run, followed by a gradual decrease toward a lower band after mid-trajectory (Figure 4c). CPD2-6QFQ maintained a comparable compactness regime with modest fluctuations and a tendency to occupy a marginally higher band later in the trajectory. Because Rg tracks the mass-weighted distribution of atoms around the molecular centroid, these trends suggest minor ligand-dependent differences in global breathing rather than major folding or unfolding transitions [31].

H-bond counts fluctuated in a predominantly sparse regime for both systems, most frequently around 0-1 with intermittent short-lived excursions to higher counts. CPD2-6QFQ displayed a denser cluster of higher-count events in the mid-trajectory region, including a rare spike reaching 4, whereas Belzutifan-6QFQ showed recurrent but generally lower excursions,

reaching 3 at maximum (Figure 4d). Such intermittency aligns with the dynamic nature of hydrogen-bond assignment under geometric criteria and the known propensity for ligand-protein polar contacts to form and break during side-chain reorientation and water-mediated rearrangements. A higher frequency of transient Hbonds may indicate episodic polar anchoring that coexists with a hydrophobic/dispersion-dominated binding groove, rather than a single permanent H-bond lock [23].

SASA traces for both complexes occupied a relatively narrow band (roughly 80-93 nm^2), consistent with stable overall solvent exposure during the 100 ns window. Belzutifan-6QFQ sampled higher SASA values more frequently in the early-to-mid phase, followed by a shift toward lower SASA after 60 ns, suggesting reduced exposure and a somewhat more compact solvent-facing ensemble in the later period. CPD2-6QFQ showed persistent fluctuations with a mild tendency to remain higher than the Belzutifan-bound state during late times, paralleling the late-stage Rg behavior (Figure 4e). Since SASA reflects exposure of protein surface to solvent and often correlates with breathing motions and pocket accessibility, the observed divergence after mid-trajectory supports ligand-dependent modulation of surface exposure without evidence for large-scale unfolding [32].

Across RMSD, RMSF, Rg, Hbonds, and SASA, both CPD2-6QFQ and Belzutifan-6QFQ exhibited stable dynamical behavior over 100 ns, with differences expressed mainly as modest shifts in solvent exposure and the frequency of transient Hbonds. Such a stability signature supports continued downstream validation using endpoint-free energy approaches and contact-persistence mapping, consistent with recommended multi-stage in silico workflows for protein-ligand systems and for BH3-groove contexts, where subtle conformational adaptation can influence ranking. From a mechanistic perspective, these MD observations are more consistent with maintenance of a dynamically tolerated bound state than with evidence of exceptionally strong binding. The generally sparse and fluctuating hydrogen-bond pattern, together with stable backbone behavior, supports the view that hydrophobic accommodation may contribute more strongly than persistent polar anchoring in this system. Because the analysis was based on a single trajectory per complex, these observations should be interpreted cautiously.

3.3. Free binding energy (MMGBSA) analysis.

Molecular Mechanics Generalized Born Surface Area (MMGBSA) is a powerful, intermediate-accuracy computational method widely used in drug discovery and natural product research to estimate the binding free energy of protein-ligand complexes. It provides a balance between the speed of docking and the accuracy of rigorous thermodynamic simulations, allowing researchers to rank and validate natural compounds from databases for therapeutic potential. This method is commonly reported as an enthalpy-like estimate derived from molecular mechanics terms plus continuum-solvation contributions, while configurational entropy is often omitted for ranking because entropy estimation can be noisy and protocol-dependent [33,34]. Consistent with standard decomposition, the gas-phase contribution is summarized as $\Delta G\_GAS = \Delta VDWAALS + \Delta EEL$, and the solvation term as $\Delta G\_SOLV = \Delta EGB + \Delta ESURF$, where ΔEGB typically penalizes burial of polar groups, and $\Delta ESURF$ approximates nonpolar solvation using surface-area-based models. The use of the CHARMM36 family of force fields for the underlying molecular dynamics ensemble is consistent with broad deployment in biomolecular simulations and in binding-energy post-

processing [35]. The binding free energies obtained from MMGBSA calculations for the CPD2-6QFQ and Belzutifan-6QFQ complexes are shown in Table 2.

Table 2. Free energy of binding obtained using MMGBSA calculations.

Energy Component	Average (kcal/mol)		Standard Deviation	
	CPD2-6QFQ	Belzutifan-6QFQ	CPD2-6QFQ	Belzutifan-6QFQ
ΔVDWAALS	-42.90	-32.37	3.96	3.42
ΔEEL	-3.66	-15.12	9.56	7.16
ΔEGB	15.66	30.12	7.95	5.57
ΔESURF	-5.11	-4.48	0.45	0.46
ΔGGAS	-46.56	-47.50	9.52	7.84
ΔGSOLV	10.55	25.64	8.00	5.43
ΔTOTAL	-36.01	-21.85	4.21	3.43

CPD2-6QFQ showed a markedly more favorable mean ΔTOTAL (-36.01 ± 4.21 kcal/mol) than Belzutifan-6QFQ (-21.85 ± 3.43 kcal/mol), suggesting a more favorable predicted binding tendency for CPD2 within the same computational protocol [36]. The primary driver of this separation was the nonpolar/dispersion-dominated term: ΔVDWAALS was substantially more favorable for CPD2 (-42.90 ± 3.96 kcal/mol) than for Belzutifan (-32.37 ± 3.42 kcal/mol), consistent with the frequent dominance of van der Waals packing in groove-like pockets when shape complementarity and hydrophobic burial are prominent [37].

Electrostatics displayed the opposite trend. Belzutifan exhibited a more favorable Coulombic term (ΔEEL = -15.12 ± 7.16 kcal/mol) than CPD2 (ΔEEL = -3.66 ± 9.56 kcal/mol), suggesting stronger gas-phase charge-charge attraction for the reference ligand. However, the electrostatic advantage for Belzutifan was counterbalanced by a much larger polar-solvation penalty (ΔEGB = 30.12 ± 5.57 kcal/mol) relative to CPD2 (ΔEGB = 15.66 ± 7.95 kcal/mol), reflecting the typical MMGBSA pattern in which enhanced Coulombic attraction is partially or fully canceled by desolvation costs captured by generalized Born models [38]. Nonpolar solvation (ΔESURF) contributed favorably in both complexes and differed only modestly (CPD2: -5.11 ± 0.45 kcal/mol; Belzutifan: -4.48 ± 0.46 kcal/mol), consistent with SASA-based models acting as a smaller compensatory term compared with ΔEGB in many protein-ligand systems [39,40].

Inspection of aggregated terms reinforced the same energetic balance. Gas-phase stabilization was similar in magnitude for both complexes (ΔG_GAS: -46.56 ± 9.52 kcal/mol for CPD2; -47.50 ± 7.84 kcal/mol for Belzutifan), with Belzutifan marginally more favorable in ΔG_GAS due to the stronger ΔEEL. In contrast, solvation opposed binding far more strongly for Belzutifan (ΔG_SOLV = 25.64 ± 5.43 kcal/mol) than for CPD2 (ΔG_SOLV = 10.55 ± 8.00 kcal/mol), producing the observed advantage in ΔTOTAL for CPD2. This balance, nonpolar packing plus reduced polar-desolvation cost, outweighing electrostatic attraction, aligns with benchmarking studies showing that MMGBSA rankings are governed by compensation between ΔG_GAS and ΔG_SOLV and remain most interpretable as within-protocol, relative comparisons [41].

From a variability standpoint, ΔTOTAL showed moderate dispersion in both systems (4.21 kcal/mol for CPD2; 3.43 kcal/mol for Belzutifan), supporting reasonably stable energetic estimates across the analyzed snapshots, with slightly higher fluctuations for CPD2. Such dispersion is consistent with the sensitivity of end-point methods to conformational sampling. It emphasizes the need for interpreting molecular dynamics stability descriptors alongside molecular dynamics stability descriptors rather than treating them as standalone surrogates for experimental affinity. Overall, MMGBSA decomposition suggests that CPD2-6QFQ has a more favorable estimated binding profile than Belzutifan-6QFQ, driven mainly by enhanced

ΔVDWAALS and a substantially reduced ΔEGB/ΔG_SOLV penalty, despite weaker Coulombic attraction (ΔEEL). This energetic pattern suggests that the predicted advantage of CPD2 is primarily associated with nonpolar packing and reduced desolvation costs rather than stronger electrostatic stabilization. In conceptual terms, such a balance is compatible with groove-shaped binding environments in which shape complementarity and hydrophobic burial dominate the overall interaction profile. However, these MMGBSA values should be interpreted as relative estimates within a single computational protocol rather than absolute binding free energies, because end-point methods remain sensitive to conformational sampling, force-field selection, and implicit-solvent settings. Moreover, entropic contributions were not explicitly included, and the calculations were derived from a single MD trajectory for each complex.

3.4. ADMET prediction analysis.

It is widely recognized that employing computational ADMET in combination with in vivo and in vitro predictions as early as possible in the drug discovery process is essential to reduce safety issues, minimize late-stage attrition, and lower the costs of bringing new drugs to market [42]. Accordingly, ADMET profiling was conducted to compare the developability-relevant pharmacokinetic and toxicological characteristics of CPD2 with those of Belzutifan using the pkCSM framework, which is based on graph-derived molecular signatures for multi-endpoint prediction. The predicted ADMET results are presented in Table 3.

Table 3. Predicted ADMET properties of CPD2 and Belzutifan.

ADMET properties	Unit	CPD2	Belzutifan
Water Solubility	(Log mol/L)	-5.258	-4.733
Caco2 permeability	(Log Papp in 10^{-6} cm/s)	0.805	1.282
Intestinal absorption (Human)	(% Absorbed)	82.48	92.996
Skin permeability	(Log Kp)	-3.228	-2.784
P-glycoprotein substrate	Yes/No	Yes	No
P-glycoprotein I inhibitor	Yes/No	Yes	Yes
P-glycoprotein II inhibitor	Yes/No	No	No
VDss	(Log L/kg)	-0.036	0.684
Fraction unbound (human)	(Fu)	0.176	0.014
BBB permeability	(Log BB)	-0.919	-1.105
CNS permeability	(Log PS)	-3.087	-3.167
CYP2D6 substrate	Yes/No	No	No
CYP3A4 substrate	Yes/No	Yes	Yes
CYP1A2 inhibitor	Yes/No	No	Yes
CYP2C19 inhibitor	Yes/No	No	Yes
CYP2C9 inhibitor	Yes/No	No	Yes
CYP2D6 inhibitor	Yes/No	No	No
CYP3A4 inhibitor	Yes/No	No	No
Total clearance	(Log ml/min/kg)	0.322	0.291
Renal OCT2 substrate	Yes/No	No	No
AMES toxicity	Yes/No	**Yes**	**No**
Maximum tolerated dose (human)	(Log mg/kg/day)	-0.956	0.291
hERG I inhibitor	Yes/No	No	No
hERG II inhibitor	Yes/No	No	No
Oral rat acute toxicity (LD50)	(mol/kg)	3.357	2.775
Oral rat chronic toxicity (LOAEL)	(Log mg/kg_bw/day)	1.942	0.892
Hepatotoxicity	Yes/No	No	Yes
Skin sensation	Yes/No	No	No
Tetrahymena pyriformis toxicity	(Log ug/L)	0.293	0.419
Minnow toxicity	(Log mM)	1.792	1.344

Predicted aqueous solubility was lower for CPD2 than for Belzutifan (-5.258 vs -4.733 log mol/L), indicating a stronger modeled solubility limitation for CPD2. Permeability-related

descriptors also favored Belzutifan, with higher predicted Caco-2 permeability (1.282 vs 0.805 log Papp in 10^{-6} cm/s) and higher predicted human intestinal absorption (92.996% vs 82.48%) [43]. Both compounds showed negative skin permeability values (logKp), with Belzutifan presenting a less negative value than CPD2 (-2.784 vs -3.228), consistent with relatively higher modeled skin permeation for Belzutifan within the same prediction scale. Transporter-related annotations distinguished the two candidates more clearly: CPD2 was predicted as a P-glycoprotein substrate, whereas Belzutifan was not; both compounds were predicted as P-glycoprotein I inhibitors, and neither compound was predicted as a P-glycoprotein II inhibitor [44]. This pattern is relevant because transporter substrate/inhibitor status may influence intestinal efflux behavior and the risk of transporter-mediated interactions.

Distribution predictions suggested broader tissue distribution for Belzutifan, based on a higher VDss value (0.684 vs -0.036 log L/kg). In contrast, the predicted human fraction unbound was substantially higher for CPD2 than for Belzutifan (0.176 vs 0.014), indicating a larger modeled unbound circulating fraction for CPD2. Central distribution indices remained low for both compounds, with negative values for both BBB permeability and CNS permeability (logBB/logPS) [45]. However, CPD2 showed slightly less negative values than Belzutifan (logBB: -0.919 vs -1.105; logPS: -3.087 vs -3.167), which is consistent with marginally higher modeled brain access for CPD2 within the same prediction framework, although both profiles still support limited central exposure overall.

Metabolism-related outputs indicated a shared substrate pattern for the two compounds, with both predicted as CYP3A4 substrates and CYP2D6 non-substrates. A divergence emerged in CYP inhibition endpoints [46]. CPD2 was predicted to be negative for inhibition of CYP1A2, CYP2C19, CYP2C9, CYP2D6, and CYP3A4, whereas Belzutifan was predicted to inhibit CYP1A2, CYP2C19, and CYP2C9, while remaining negative for CYP2D6 and CYP3A4 inhibition. Within the scope of these in silico endpoints, CPD2 therefore presents a comparatively cleaner CYP inhibition profile. At the same time, Belzutifan carries broader modeled CYP inhibition liabilities that may warrant focused interaction assessment during follow-up studies.

Predicted excretion properties showed only a small difference in total clearance, with CPD2 having a slightly higher predicted total clearance than Belzutifan (0.322 vs 0.291 log ml/min/kg), suggesting modestly faster overall elimination for CPD2 under model assumptions. Both compounds were predicted as non-substrates of renal OCT2, indicating no endpoint-level distinction in OCT2-mediated renal transport liability in this comparison.

Toxicity predictions revealed several meaningful differences between the two candidates. CPD2 was predicted to be AMES-positive, whereas Belzutifan was AMES-negative, generating a mutagenicity alert for CPD2 in this screening context. Predicted human maximum tolerated dose was lower for CPD2 than for Belzutifan (-0.956 vs 0.291 log mg/kg/day), indicating lower modeled dose tolerance for CPD2 on this endpoint. Cardiac liability predictions were favorable for both compounds in the pkCSM panel, with negative predictions for both hERG I and hERG II inhibition [47]. Rodent toxicity descriptors also differed numerically. CPD2 showed a higher predicted oral rat acute toxicity LD50 than Belzutifan (3.357 vs 2.775 mol/kg), indicating a lower modeled acute toxicity concern for CPD2 on this endpoint. CPD2 also showed a higher predicted oral rat chronic toxicity LOAEL than Belzutifan (1.942 vs 0.892 log mg/kg_bw/day), indicating a less adverse modeled chronic toxicity threshold for CPD2 relative to Belzutifan within the same prediction scale. Hepatotoxicity predictions diverged in the opposite direction, with CPD2 predicted as non-

hepatotoxic and Belzutifan predicted as hepatotoxic [48]. Skin sensitization was predicted to be negative for both compounds. Ecotoxicity-related endpoints further separated the two profiles. CPD2 showed a lower predicted *Tetrahymena pyriformis* toxicity value than Belzutifan (0.293 vs 0.419 log µg/L), while CPD2 showed a higher predicted minnow toxicity value than Belzutifan (1.792 vs 1.344 log mM). These differences support endpoint-level discrimination between the two compounds, although mechanistic interpretation should remain conservative, given that the endpoints represent distinct biological systems and measurement scales.

Collectively, the pkCSM outputs suggest that Belzutifan has a more favorable modeled absorption profile than CPD2, with higher predicted aqueous solubility, Caco-2 permeability, and intestinal absorption, and also a higher predicted VDss consistent with broader tissue distribution. CPD2, in contrast, shows a substantially higher predicted unbound fraction and slightly lower BBB/CNS permeability indices. However, both compounds remain within a low-penetration range and a cleaner CYP inhibition profile across the evaluated isoforms. Excretion-related predictions show only a minor difference in clearance and no OCT2-substrate signal for either compound. The principal developability concern for CPD2 in this panel is the AMES-positive prediction, together with a lower predicted human maximum tolerated dose. In contrast, Belzutifan carries predicted hepatotoxicity and broader CYP inhibition liabilities despite an AMES-negative profile. These findings support prioritization of confirmatory genotoxicity testing for CPD2, liver-safety assessment for Belzutifan, and experimental ADME validation for both candidates during subsequent optimization. Accordingly, the ADMET profile does not support an unambiguously favorable developability assessment for CPD2. Instead, the compound presents a trade-off pattern in which a cleaner CYP inhibition profile and absence of predicted hepatotoxicity are counterbalanced by weaker modeled absorption and an AMES mutagenicity alert. This balance supports cautious prioritization rather than straightforward advancement.

4. Conclusions

This study provides a multi-level computational framework for prioritizing selected withanolides from *P. philadelphica* as putative modulators of the anti-apoptotic protein Mcl-1 (PDB: 6QFQ), using Belzutifan as a reference. Among the selected compounds, CPD2 showed the most favorable docking score (-11.11 kcal/mol) relative to Belzutifan (-9.48 kcal/mol) and the remaining ligands, with a pocket-spanning interaction pattern dominated by van der Waals and hydrophobic contacts in the BH3-groove region. Molecular dynamics simulations supported conformational stability of both CPD2-6QFQ and Belzutifan-6QFQ complexes, with backbone RMSD maintained within a narrow range (0.08-0.16 nm), stable compactness (Rg of 1.42-1.47 nm), limited residue-level fluctuations, and no evidence of large-scale structural destabilization. MMGBSA analysis further supported a more favorable estimated binding profile for CPD2 than for Belzutifan (ΔTOTAL = -36.01 ± 4.21 vs -21.85 ± 3.43 kcal/mol), driven mainly by a more favorable van der Waals term (ΔVDWAΔALS = -42.90 ± 3.96 vs -32.37 ± 3.42 kcal/mol) and a lower solvation penalty (ΔGSOLV = 10.55 ± 8.00 vs 25.64 ± 5.43 kcal/mol). ADMET profiling indicated a mixed developability profile for CPD2, including favorable CYP inhibition predictions but an AMES-positive mutagenicity alert.

Current findings should be interpreted as an early computational prioritization signal rather than definitive evidence of therapeutic utility, since all reported outcomes arise from in silico models and remain influenced by methodological assumptions and parameter settings.

Empirical validation is required to verify direct Mcl-1 engagement, inhibitory activity at the target level, and anticancer effects in renal adenocarcinoma-relevant biological systems. Key next-stage studies should include biophysical and biochemical binding assays, functional Mcl-1 inhibition experiments, cell-based apoptosis and viability analyses, selectivity assessment across the Bcl-2 family, and expanded pharmacokinetic and safety characterization, with particular attention to confirmatory genotoxicity testing for CPD2. If supported by subsequent in vitro and in vivo results, CPD2 could be advanced as a lead framework for optimization and preclinical development.

Author Contributions

Conceptualization, H.D.N.; investigation, H.D.N.; writing-original draft preparation, H.D.N.; visualization, H.D.N. The author has read and agreed to the published version of the manuscript.

Institutional Review Board Statement

Not applicable.

Informed Consent Statement

Not applicable.

Data Availability Statement

Data supporting the findings of this study are available upon reasonable request from the corresponding author.

Funding

This research received no external funding.

Acknowledgments

The contributors to this work, whether directly or indirectly, have our sincere gratitude.

Conflicts of Interest

The author declares no conflict of interest.

References

1. Cardenas, L.M.; Sigurdson, S.; Wallis, C.J.D.; Lalani, A.K.; Swaminath, A. Advances in the management of renal cell carcinoma. *Can. Med. Assoc. J.* **2024**, *196*, E235-E240, https://doi.org/10.1503/cmaj.230356.
2. Semenescu, L.E.; Kamel, A.; Ciubotaru, V.; Baez-Rodriguez, S.M.; Furtos, M.; Costachi, A.; Dricu, A.; Tătăranu, L.G. An Overview of Systemic Targeted Therapy in Renal Cell Carcinoma, with a Focus on Metastatic Renal Cell Carcinoma and Brain Metastases. *Curr. Issues Mol. Biol.* **2023**, *45*, 7680-7704, https://doi.org/10.3390/cimb45090485.
3. Garg, P.; Pareek, S.; Kulkarni, P.; Horne, D.; Salgia, R.; Singhal, S.S. Next-Generation Immunotherapy: Advancing Clinical Applications in Cancer Treatment. *J. Clin. Med.* **2024**, *13*, 6537, https://doi.org/10.3390/jcm13216537.
4. Chen, A.H.; Grana, A.K. Belzutifan's role in the treatment landscape of clear cell renal cell carcinoma. *Pharmacotherapy: J. Human Pharmacol. Drug Ther.* **2025**, *45*, 356-366,

https://doi.org/10.1002/phar.70023.
5. Kowalewski, A.; Borowczak, J.; Maniewski, M.; Gostomczyk, K.; Grzanka, D.; Szylberg, Ł. Targeting apoptosis in clear cell renal cell carcinoma. *Biomed. Pharmacother.* **2024**, *175*, 116805, https://doi.org/10.1016/j.biopha.2024.116805.
6. Negi, A.; Murphy, P.V. Development of Mcl-1 inhibitors for cancer therapy. *Eur. J. Med. Chem.* **2021**, *210*, 113038, https://doi.org/10.1016/j.ejmech.2020.113038.
7. Mohiuddin, M. Targeting MCL-1 to Overcome Therapeutic Resistance and Improve Cancer Mortality. *Health Sci. Rep.* **2025**, *8*, e71390, https://doi.org/10.1002/hsr2.71390.
8. Singh, A.; Raza, A.; Amin, S.; Damodaran, C.; Sharma, A.K. Recent Advances in the Chemistry and Therapeutic Evaluation of Naturally Occurring and Synthetic Withanolides. *Molecules* **2022**, *27*, 886, https://doi.org/10.3390/molecules27030886.
9. Zhang, Q.; Yuan, Y.; Cao, S.; Kang, N.; Qiu, F. Withanolides: Promising candidates for cancer therapy. *Phyther. Res.* **2024**, *38*, 1104-1158, https://doi.org/10.1002/ptr.8090.
10. Xu, Y.-M.; Wijeratne, E.M.K.; Brooks, A.D.; Tewary, P.; Xuan, L.-J.; Wang, W.-Q.; Sayers, T.J.; Gunatilaka, A.A.L. Cytotoxic and other withanolides from aeroponically grown *Physalis philadelphica*. *Phytochemistry* **2018**, *152*, 174-181, https://doi.org/10.1016/j.phytochem.2018.04.018.
11. Murray, J.B.; Davidson, J.; Chen, I.; Davis, B.; Dokurno, P.; Graham, C.J.; Harris, R.; Jordan, A.; Matassova, N.; Pedder, C.; Ray, S.; Roughley, S.D.; Smith, J.; Walmsley, C.; Wang, Y.; Whitehead, N.; Williamson, D.S.; Casara, P.; Le Diguarher, T.; Hickman, J.; Stark, J.; Kotschy, A.; Geneste, O.; Hubbard, R.E. Establishing Drug Discovery and Identification of Hit Series for the Anti-apoptotic Proteins, Bcl-2 and Mcl-1. *ACS Omega* **2019**, *4*, 8892-8906, https://doi.org/10.1021/acsomega.9b00611.
12. Van Der Spoel, D.; Lindahl, E.; Hess, B.; Groenhof, G.; Mark, A.E.; Berendsen, H.J.C. GROMACS: Fast, flexible, and free. *J. Comput. Chem.* **2005**, *26*, 1701-1718, https://doi.org/10.1002/jcc.20291.
13. Guex, N.; Peitsch, M.C. SWISS-MODEL and the Swiss-Pdb Viewer: An environment for comparative protein modeling. *ELECTROPHORESIS* **1997**, *18*, 2714-2723, https://doi.org/10.1002/elps.1150181505.
14. Zoete, V.; Cuendet, M.A.; Grosdidier, A.; Michielin, O. SwissParam: A fast force field generation tool for small organic molecules. *J. Comput. Chem.* **2011**, *32*, 2359-2368, https://doi.org/10.1002/jcc.21816.
15. Pettersen, E.F.; Goddard, T.D.; Huang, C.C.; Couch, G.S.; Greenblatt, D.M.; Meng, E.C.; Ferrin, T.E. UCSF Chimera—A visualization system for exploratory research and analysis. *J. Comput. Chem.* **2004**, *25*, 1605-1612, https://doi.org/10.1002/jcc.20084.
16. Pires, D.E.V; Blundell, T.L.; Ascher, D.B. pkCSM: Predicting Small-Molecule Pharmacokinetic and Toxicity Properties Using Graph-Based Signatures. *J. Med. Chem.* **2015**, *58*, 4066-4072, https://doi.org/10.1021/acs.jmedchem.5b00104.
17. Sharma, P.; Sharma, K.; Nandave, M. Chapter 2 - Computational approaches in drug discovery and design. In Computational Approaches in Drug Discovery, Development and Systems Pharmacology, Gautam, R.K., Kamal, M.A., Mittal, P., Eds.; Academic Press: **2023**; pp. 53-93, https://doi.org/10.1016/B978-0-323-99137-7.00009-5.
18. Delbridge, A.R.D.; Strasser, A. The BCL-2 protein family, BH3-mimetics and cancer therapy. *Cell Death Differ.* **2015**, *22*, 1071-1080, https://doi.org/10.1038/cdd.2015.50.
19. Che, X.; Liu, Q.; Zhang, L. An accurate and universal protein-small molecule batch docking solution using Autodock Vina. *Results Eng.* **2023**, *19*, 101335, https://doi.org/10.1016/j.rineng.2023.101335.
20. Shirali, A.; Stebliankin, V.; Karki, U.; Shi, J.; Chapagain, P.; Narasimhan, G. A comprehensive survey of scoring functions for protein docking models. *BMC Bioinformatics* **2025**, *26*, 25, https://doi.org/10.1186/s12859-024-05991-4.
21. Bolomsky, A.; Vogler, M.; Köse, M.C.; Heckman, C.A.; Ehx, G.; Ludwig, H.; Caers, J. MCL-1 inhibitors, fast-lane development of a new class of anti-cancer agents. *J. Hematol. Oncol.* **2020**, *13*, 173, https://doi.org/10.1186/s13045-020-01007-9.
22. Sun, Q. The Hydrophobic Effects: Our Current Understanding. *Molecules* **2022**, *27*, 7009, https://doi.org/10.3390/molecules27207009.
23. Ferreira de Freitas, R.; Schapira, M. A systematic analysis of atomic protein–ligand interactions in the PDB. *Med. Chem. Commun.* **2017**, *8*, 1970-1981, https://doi.org/10.1039/C7MD00381A.
24. Chen, W.; He, H.; Wang, J.; Wang, J.; Chang, C.A. Uncovering water effects in protein–ligand recognition: importance in the second hydration shell and binding kinetics. *Phys. Chem. Chem. Phys.* **2023**, *25*, 2098-2109, https://doi.org/10.1039/D2CP04584B.
25. Fallah, J.; Brave, M.H.; Weinstock, C.; Mehta, G.U.; Bradford, D.; Gittleman, H.; Bloomquist, E.W.;

Charlab, R.; Hamed, S.S.; Miller, C.P.; Dorff, S.E.; Chambers, W.A.; Mixter, B.D.; Dinin, J.; Pierce, W.F.; Ricks, T.K.; Tang, S.; Donoghue, M.; Pazdur, R.; Amiri-Kordestani, L.; Ibrahim, A.; Beaver, J.A. FDA Approval Summary: Belzutifan for von Hippel-Lindau Disease–Associated Tumors. *Clin. Cancer Res.* **2022**, *28*, 4843-4848, https://doi.org/10.1158/1078-0432.CCR-22-1054.

26. Wu, X.; Lazris, D.; Wong, R.; Tykodi, S.S. Belzutifan for the treatment of renal cell carcinoma. *Ther. Adv. Med. Oncol.* **2025**, *17*, 17588359251317846, https://doi.org/10.1177/17588359251317846.
27. Du, X.; Li, Y.; Xia, Y.-L.; Ai, S.-M.; Liang, J.; Sang, P.; Ji, X.-L.; Liu, S.-Q. Insights into Protein–Ligand Interactions: Mechanisms, Models, and Methods. *Int. J. Mol. Sci.* **2016**, *17*, 144, https://doi.org/10.3390/ijms17020144.
28. Aghajani, J.; Farnia, P.; Farnia, P.; Ghanavi, J.; Velayati, A.A. Molecular Dynamic Simulations and Molecular Docking as a Potential Way for Designed New Inhibitor Drug without Resistance. *Tanaffos* **2022**, *21*, 1-14.
29. Borjian Boroujeni, M.; Shahbazi Dastjerdeh, M.; Shokrgozar, M.; Rahimi, H.; Omidinia, E. Computational driven molecular dynamics simulation of keratinocyte growth factor behavior at different pH conditions. *Inform. Med. Unlocked* **2021**, *23*, 100514, https://doi.org/10.1016/j.imu.2021.100514.
30. Wolf, E.; Lento, C.; Pu, J.; Dickinson, B.C.; Wilson, D.J. Innate Conformational Dynamics Drive Binding Specificity in Anti-Apoptotic Proteins Mcl-1 and Bcl-2. *Biochemistry* **2023**, *62*, 1619-1630, https://doi.org/10.1021/acs.biochem.2c00709.
31. Kufareva, I.; Abagyan, R. Methods of Protein Structure Comparison. In Homology Modeling: Methods and Protocols, Orry, A.J.W., Abagyan, R., Eds.; Humana Press: Totowa, NJ, **2012**; pp. 231-257, https://doi.org/10.1007/978-1-61779-588-6_10.
32. Savojardo, C.; Manfredi, M.; Martelli, P.L.; Casadio, R. Solvent Accessibility of Residues Undergoing Pathogenic Variations in Humans: From Protein Structures to Protein Sequences. *Front. Mol. Biosci.* **2021**, *7*, 626363, https://doi.org/10.3389/fmolb.2020.626363.
33. Valdés-Tresanco, M.S.; Valdés-Tresanco, M.E.; Valiente, P.A.; Moreno, E. gmx_MMPBSA: A New Tool to Perform End-State Free Energy Calculations with GROMACS. *J. Chem. Theory Comput.* **2021**, *17*, 6281-6291, https://doi.org/10.1021/acs.jctc.1c00645.
34. Akkus, E.; Tayfuroglu, O.; Yildiz, M.; Kocak, A. Accurate Binding Free Energy Method from End-State MD Simulations. *J. Chem. Inf. Model.* **2022**, *62*, 4095-4106, https://doi.org/10.1021/acs.jcim.2c00601.
35. Vanommeslaeghe, K.; MacKerell Jr., A.D. CHARMM additive and polarizable force fields for biophysics and computer-aided drug design. *Biochim. Biophys. Acta - Gen. Subj.* **2015**, *1850*, 861-871, https://doi.org/10.1016/j.bbagen.2014.08.004.
36. Wang, S.; Sun, X.; Cui, W.; Yuan, S. MM/PB(GB)SA benchmarks on soluble proteins and membrane proteins. *Front. Pharmacol.* **2022**, *13*, 1018351, https://doi.org/10.3389/fphar.2022.1018351.
37. Dasmahapatra, U.; Kumar, C.K.; Das, S.; Subramanian, P.T.; Murali, P.; Isaac, A.E.; Ramanathan, K.; Mm, B.; Chanda, K. *In-silico* molecular modelling, MM/GBSA binding free energy and molecular dynamics simulation study of novel pyrido fused imidazo[4,5-*c*]quinolines as potential anti-tumor agents. *Front. Chem.* **2022**, *10*, 991369, https://doi.org/10.3389/fchem.2022.991369.
38. Onufriev, A.V; Case, D.A. Generalized Born Implicit Solvent Models for Biomolecules. *Annu. Rev. Biophys.* **2019**, *48*, 275-296, https://doi.org/10.1146/annurev-biophys-052118-115325.
39. Dong, L.; Li, P.; Wang, B. Enhancing MM/P(G)BSA Methods: Integration of Formulaic Entropy for Improved Binding Free Energy Calculations. *J. Comput. Chem.* **2025**, *46*, e70093, https://doi.org/10.1002/jcc.70093.
40. Hou, T.; Wang, J.; Li, Y.; Wang, W. Assessing the Performance of the MM/PBSA and MM/GBSA Methods. 1. The Accuracy of Binding Free Energy Calculations Based on Molecular Dynamics Simulations. *J. Chem. Inf. Model.* **2011**, *51*, 69-82, https://doi.org/10.1021/ci100275a.
41. Bello, M.; Bandala, C. Evaluating the ability of end-point methods to predict the binding affinity tendency of protein kinase inhibitors. *RSC Adv.* **2023**, *13*, 25118-25128, https://doi.org/10.1039/D3RA04916G.
42. Pradeepkiran, J.A.; Sainath, S.B.; Shrikanya, K.V.L. Chapter 5 - In silico validation and ADMET analysis for the best lead molecules. In Brucella Melitensis, Pradeepkiran, J.A., Sainath, S.B., Eds.; Academic Press: **2021**; pp. 133-176, https://doi.org/10.1016/B978-0-323-85681-2.00008-2.
43. Falcón-Cano, G.; Molina, C.; Cabrera-Pérez, M.Á. Reliable Prediction of Caco-2 Permeability by Supervised Recursive Machine Learning Approaches. *Pharmaceutics* **2022**, *14*, 1998, https://doi.org/10.3390/pharmaceutics14101998.
44. Veiga-Matos, J.; Morales, A.I.; Prieto, M.; Remião, F.; Silva, R. Study Models of Drug–Drug Interactions

Involving P-Glycoprotein: The Potential Benefit of P-Glycoprotein Modulation at the Kidney and Intestinal Levels. *Molecules* **2023**, *28*, 7532, https://doi.org/10.3390/molecules28227532.
45. Stéen, E.J.L.; Vugts, D.J.; Windhorst, A.D. The Application of in silico Methods for Prediction of Blood-Brain Barrier Permeability of Small Molecule PET Tracers. *Front. Nucl. Med.* **2022**, *2*, 853475, https://doi.org/10.3389/fnume.2022.853475.
46. Guengerich, F.P. Chapter One - Roles of cytochrome P450 enzymes in pharmacology and toxicology: Past, present, and future. In Advances in Pharmacology, Yamazaki, H., Ed.; Academic Press: **2022**; Volume 95, pp. 1-47, https://doi.org/10.1016/bs.apha.2021.12.001.
47. Goel, H.; Yu, W.; MacKerell Jr, A.D. hERG Blockade Prediction by Combining Site Identification by Ligand Competitive Saturation and Physicochemical Properties. *Chemistry* **2022**, *4*, 630-646, https://doi.org/10.3390/chemistry4030045.
48. Shin, H.K.; Huang, R.; Chen, M. *In silico* modeling-based new alternative methods to predict drug and herb-induced liver injury: A review. *Food Chem. Toxicol.* **2023**, *179*, 113948, https://doi.org/10.1016/j.fct.2023.113948.

Publisher's Note & Disclaimer

The statements, opinions, and data presented in this publication are solely those of the individual author(s) and contributor(s) and do not necessarily reflect the views of the publisher and/or the editor(s). The publisher and/or the editor(s) disclaim any responsibility for the accuracy, completeness, or reliability of the content. Neither the publisher nor the editor(s) assume any legal liability for any errors, omissions, or consequences arising from the use of the information presented in this publication. Furthermore, the publisher and/or the editor(s) disclaim any liability for any injury, damage, or loss to persons or property that may result from the use of any ideas, methods, instructions, or products mentioned in the content. Readers are encouraged to independently verify any information before relying on it, and the publisher assumes no responsibility for any consequences arising from the use of materials contained in this publication.